# High-resolution imaging algorithms for automotive radar challenges in real driving scenarios

Yuan, Sen; Fioranelli, Francesco; Yarovoy, Alexander

**DOI**
10.1109/MAES.2025.3550301

**Publication date**
2025

**Document Version**
Final published version

**Published in**
IEEE Aerospace and Electronic Systems Magazine

Feature Articles:

DOI. No. 10.1109/MAES.2025.3550301

# High-Resolution Imaging Algorithms for Automotive Radar: Challenges in Real Driving Scenarios

*Sen Yuan*, *Francesco Fioranelli*, *and Alexander Yarovoy*, **Delft University of Technology, 2628 CD Delft, The Netherlands**

## INTRODUCTION

Radar provides robust sensing ability in range–Doppler–azimuth–elevation domains regardless of the weather or light conditions; hence, it has been one of the "must" technologies in automotive. To provide comprehensive and accurate information on vehicle surroundings for subsequent perception tasks, radar is required to provide high-resolution data (i.e., from a detector to an imaging sensor), posing new challenges to traditional signal processing algorithms.

Because of their high degree of integration and relatively low costs, frequency-modulated continuous wave (FMCW) automotive radars operating in the 77-GHz band are the current standard [1]. They offer a large operational bandwidth, providing sufficient range resolution. Doppler resolution is a function of chirp duration and the number of chirps used for estimation, so it is limited by the coherent observation time, with better velocity resolution achieved by operating at higher frequency [2]. Angular resolution is contingent upon the antenna aperture and thus is determined by the number and positions of the transmit and receive antenna elements, in turn, limited by the radar cost and packaging size.

Significant research effort is ongoing to propose array designs and algorithms to improve angular resolution, but, to the best of the authors' knowledge, such approaches are not always evaluated in real driving scenarios with multiple extended targets and considerable clutter in the scene of interest. The aim of this article is, therefore, to first review some of the most recent approaches for high-resolution imaging in automotive radar and then discuss important insights and open challenges for their practical implementation. Specifically, data collected in the city of Delft, The Netherlands, with a vehicle equipped with both front-looking and side-looking radars, will be used to showcase performances for the different algorithms.

Authors' current address: The authors are with Microwave Sensing, Signals and Systems (MS3) Group, Delft University of Technology, 2628 CD Delft, The Netherlands (e-mail: s.yuan-3@tudelft.nl, f.fioranelli@tudelft.nl, a.yarovoy@tudelft.nl).

Manuscript received 3 April 2024, revised 11 October 2024; accepted 7 March 2025, and ready for publication 11 March 2025.

Review handled by Alessio Balleri.



## REVIEW OF HIGH-RESOLUTION IMAGING ALGORITHMS

Multiple-input multiple-output (MIMO) radar technology exploits the spatial diversity of transmit and receive antenna arrays and has received considerable attention in automotive. Due to its ability to achieve high angular resolution with fewer antennas, MIMO has been widely exploited in the current generation of automotive radars [3]. The transmitted waveforms must be orthogonal to each other to avoid interfering with each other, either constructively or destructively. This orthogonality can be achieved in different ways, for example, by spreading waveforms in time [time-division multiplexing (TDM)] or frequency (orthogonal frequency-division multiplexing). When the transmitted signals are orthogonal, a virtual MIMO array can be created, which is the typical advantage that MIMO has over a conventional phased array, as it can perform comparably with fewer actual antenna elements. This leads to a better angular resolution overall.

In MIMO radar with a virtual uniform linear array (ULA), angle finding can be implemented via digital beamforming (DBF) [4] by performing computationally efficient fast Fourier transforms on snapshots taken across the array elements, or using computationally intensive super-resolution methods, such as minimum variance distortionless response [5], and subspace-based methods, such as multiple signal classification (MUSIC) [6], [7] and estimation of signal parameters via rational invariance techniques [8]. All these methods require an input with a sufficient number of snapshots and assume a low mutual correlation of the sources and uncorrelated (white) noise [9], [10]. To obtain an accurate estimation of the

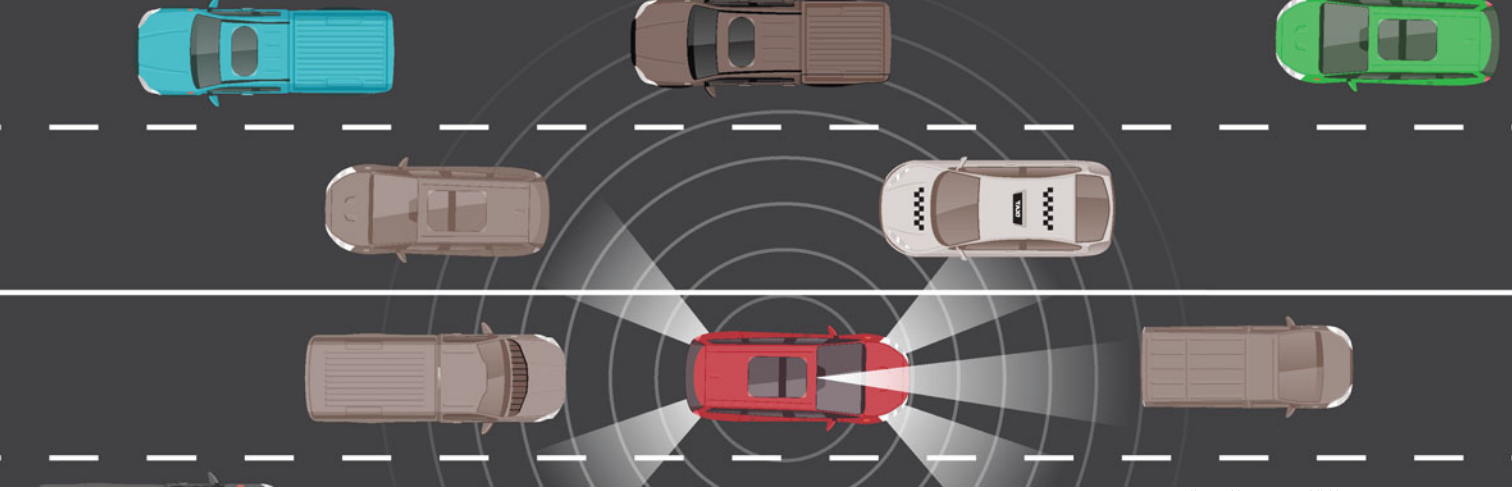

Image licensed by Ingram Publishing

array covariance matrix, spatial smoothing [6], [11] can be applied to get enough virtual snapshots.

Other methods aim to perform direction of arrival (DOA) estimation with a limited number of snapshots, which is specifically attractive in automotive radar. The modified MUSIC in [12] uses the Hankel matrix to form the autocorrelation matrix for a single snapshot case. 2D convolutional neural network has been proposed in [13] to achieve super-resolution with a single snapshot, but with results only verified in simulations. Sparse sensing-based methods [14], [15] and the iterative adaptive approach (IAA) [16], [17], [18] are potentially applicable to a single snapshot or a limited number of snapshots, but they both assume targets' sparsity and have high computational costs. Also, the Fourier interpolation methods proposed in [19] require targets' sparsity to maintain acceptable performances. The reduced signal covariance matrix proposed in [9] operates on a limited amount of snapshots with an unknown nonuniform noise but is affected by the rank deficiency problem and requires the prior number of targets. Purpose-designed arrays, such as the massive ULA in [20], focus on improving DOA estimation with a few snapshots but are designed for communication applications rather than automotive. Sparse MIMO radar arrays, as in [21], use genetic algorithms to interpolate the missing antennas in sparse arrays, but this is a computationally intensive approach.

For all the aforementioned methods, the theoretical spatial resolution is limited by the physical size of the MIMO array. The inherent motion of the vehicle provides a potential opportunity to extend the usable aperture for high-resolution automotive radar imaging. This concept has been proposed in several works, with some distinctions depending on the radar mounting position, whether forward- or side-looking.

## FORWARD-LOOKING REGIONS

It is not straightforward to exploit vehicle ego-motion for high resolution in a forward-looking direction, even if this region is very interesting in the automotive industry. First, this approach has no or poor angular resolution for look angles equal or close to zero 0°, i.e., $[-\epsilon, \epsilon]$, where $\epsilon$ indicates the angular extension of the so-called "blind zone" near the forward-looking direction [22], [23]. According to the literature, the extension of the blind zone and the Doppler bandwidth are inversely proportional: as the Doppler bandwidth increases by exploiting the movement of the vehicle, the extension of the blind zone is reduced. This has a typical value of $\epsilon = 5°$ [22], [23]. Furthermore, symmetric locations on the left/right-hand side of the vehicle trajectory have the same Doppler history, which leads to ambiguity in establishing the precise location of targets in the angular region $[-\frac{\pi}{2}, -\epsilon] \cup [\epsilon, \frac{\pi}{2}]$.

Several algorithms have been proposed in forward-looking SAR to tackle this problem. Bistatic SAR [24], [25], for example, uses another transmitter located at a different position from the receiver; in this way, the designed geometry can provide additional information to address the ambiguity problem. Frequency diverse array [26] is designed by performing transmit beamforming after range compensation, and the echo from the desired range region can be extracted from ambiguous echoes, thus providing unambiguous imaging. A multibeam Doppler beam sharpening (DBS) approach was proposed in [27] based on the DBF using a scanning imaging system to provide high cross-range resolution. Multichannel radar in [28] uses the backprojection (BP) algorithm plus MIMO information to solve the ambiguity problem, while at the same time, a curved motion trajectory can be used to improve the poor resolution in the region where look angles are equal or close to zero degrees. However, this algorithm is rather time-consuming, limiting its use in real time. Forward-looking MIMO-SAR and sparse MIMO arrays were combined in [29] with decimated BP [30] to solve the ambiguity and achieve imaging. However, these two algorithms are also rather time-consuming. A sequential spatial masking is proposed in [31] to solve the left–right ambiguity with the BP algorithm. An incoherent integration method from the MIMO and Doppler Integral was proposed in [32]. This increases cross-range resolution across the radar's field of view while suppressing sidelobe errors. However, this method has a specific requirement for vehicle movement, as it necessitates movement in the

boresight direction of the radar. An unambiguous Doppler-based forward-looking MIMO radar beam sharpening scan method [33] is proposed by combining DBS and MIMO array processing to solve the ambiguity problem of symmetric targets in forward-looking automotive radar. To make this suitable for more complicated vehicle movements and cope with the diverse reflectivity of different targets in the scene, an improved approach named "robust unambiguous DBS with adaptive threshold" (*RUDAT*) [34] is proposed. 3DRUDAT [35] is proposed later to address both ambiguities from the forward-movement geometry and the coupling between elevation and azimuth jointly from the DBS.

## SIDE-LOOKING REGIONS

Approaches forming a synthetic aperture for automotive MIMO radar have been explored in [36] and [37]. However, the methods in these studies can only enhance the resolution in their region of interest, i.e., the range of angles where targets have already been detected. Therefore, an additional processing step is needed to first detect the targets and estimate their related DOA values, which is then followed by the step of enhancing the angular resolution. To mitigate this, the method in [38] can directly image the targets in the radar field of view and use motion-enhanced snapshots coherently to reduce the computational cost of the DOA estimation. Other studies propose using the vehicle's trajectory to image the scenarios using the SAR approach. A two-radar approach is proposed in [39]: while one radar is used to determine the vehicle trajectory, another radar utilizes SAR on the known trajectory. This method uses BP, which is an imaging algorithm with a high computational load and potentially less practical use. The work in [40] uses residual motion compensation to improve the SAR image quality for automotive, but it should be noted that the aforementioned approaches still rely on snapshots across multiple frames. DBS methods are proposed for automotive radar in [32]. The velocity information was used for wideband DOA estimation with compensation of range migration and the presence of Doppler ambiguity [41], and for high angular resolution imaging [42]. Studies using neural networks have been proposed as well [43], [44], [45], [46], but despite their good results, the question of their generalization capabilities to unseen scenarios remains. Alternatively, approaches on how to create a larger virtual aperture (i.e., the sum coarray and the array aperture extension) using sensor motion under very simple scenarios have been discussed in [47] and [48]. A novel formulation of the antenna array aperture extension due to platform motion is proposed in [49]. This includes a novel expression for the steering vectors to compensate for the error from the complex motion of the vehicle, a formulation with lower computational load via an approximation in the time tag, and a signal model accounting for the variable time interval for the data acquisition periods. Also, a 3D imaging algorithm using a 1D array for automotive radar is proposed in [50], using the aforementioned concept of motion-induced snapshots that exploit the ego velocity of the vehicle.

Despite the development of many algorithms in this research field as reported in this brief review, some of them appear to be validated only on simulations, typically with ideal point targets that are not well representative of experimental data in real driving scenarios. Other algorithms are not straightforward to implement and adapt for actual automotive scenarios, for instance, because it is too computationally intensive to account for all scatter points from extended targets in dense scenes or due to variations in the point clouds returned even by the same object across subsequent frames. In the following sections, an experimental data collection with related results of high-resolution radar imaging algorithms of automotive scenes is presented. The aim of this discussion is to highlight some of the important aspects of the practical applications of such algorithms, from the settings of radar waveform parameters to the accumulation of multiple frames.

## EXPERIMENT DESCRIPTION

The radar sensors used in this data collection are the Texas Instrument MMWCAS-RF-EVM cascade radar systems, as shown in Figure 1. GPS, IMU, Lidar, and GoPro cameras are also installed on the vehicle used for the data collection, as shown in Figure 2. These sensors can provide vital information in terms of ground truth for validation of radar-only algorithms, as well as offer opportunities to develop suitable data fusion techniques at a later processing stage. Specifically, the LiDAR sensor is the RoboSense Ruby Plus Upgraded 128-beam, customized for L4 autonomous vehicle commercial operations, mounted on

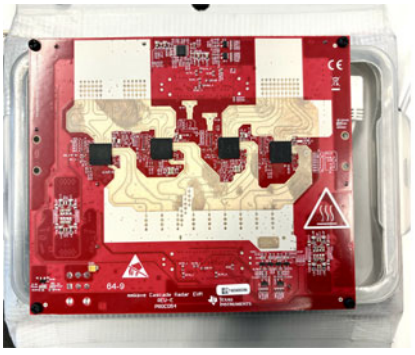

**Figure 1.**
Radar board used for radar data collection, MMWCAS-RF-EVM and MMWCAS-DSP-EVM model by Texas instrument [51].


(a)

(b)

**Figure 2.**
Vehicle used for data collection with multiple sensors mounted on it. (a) View of the vehicle and (b) zoom on the sensors mounted on the roof.

the top of the vehicle, operating at 10 Hz. This provides a maximum 250 m observation range with 0.02 m precision. The vertical field is within $[-25°, 25°]$, with up to 0.1° resolution, while the horizontal field is 360° with 0.2° resolution. Odometry information is provided by a filtered combination of several inputs: RTK GPS, IMU, and wheel odometry, with a frame rate of around 30 Hz. GPS is the industry standard GNSS/INS for ADAS and autonomous vehicle testing, RT3000 v3. Notably, as shown in Figure 2(b), two radar sensors have been used, one for the front-looking region and one for the side-looking region with respect to the driving trajectory.

## RADAR WAVEFORM PARAMETERS

A crucial step of the experimental planning consists of the design of the radar waveform and its parameters. Specifically, four operational requirements, namely, maximum unambiguous range, maximum unambiguous Doppler velocity, range resolution, and Doppler velocity resolution, play an important role in the waveform design and the subsequent sensing capabilities [52], [53], [54]. The maximum unambiguous range is determined as

$$r_{\max} = \frac{F_s c}{2\mu} \tag{1}$$

where $F_s$ is the sampling frequency for the fast time, $c$ is the speed of light, and $\mu$ is the sweeping slope of the chirp modulation equal to the ratio of the chirp bandwidth $B$ and duration of the chirp.

The maximum unambiguous Doppler velocity is determined as

$$v_{\max} = \frac{\lambda}{4T_c} \tag{2}$$

where $\lambda$ is the wavelength of the radar signal, and $T_c$ is the pulse repetition time for the chirps.

The range resolution is determined as follows:

$$r_{\text{res}} = \frac{c}{2B} \tag{3}$$

where $B$ is the bandwidth of the FMCW chirp.

The Doppler velocity resolution is determined as follows:

$$v_{\text{res}} = \frac{\lambda}{2T_c L_d} \tag{4}$$

where $L_d$ is the number of the chirps used for Doppler estimation.

Considering the required values for the aforementioned quantities, suitable waveform parameters (some of which are shown in Figure 3) can be set on the radar board. Specifically, these are the *start freq*, which is the

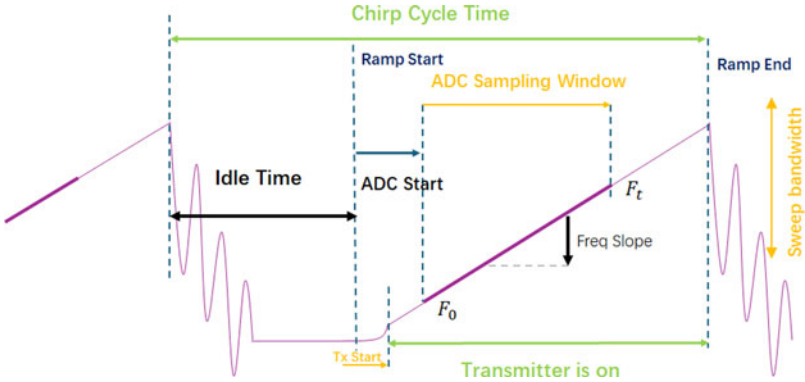


**Figure 3.**
Parameters for the radar waveform design. Figure inspired by the software used to configure the chosen radar by Texas Instrument [51].

starting frequency of the chirp, the chirp slope $\mu$, the *idle time*, which is the time needed to reset the previous chirp, the analog-to-digital converter *(ADC) start*, which is the time for reaching the starting frequency of each chirp, the *sample frequency* in fast-time $F_s$, the *ramp end time*, which is the time when the transmitter is OFF, and *adc samples*, which is the number of samples per chirp. It should be noted that $T_c$ denotes the whole chirp cycle time, including the idle time and ramp end time; the actual chirp duration will be determined by the subtraction between the ramp end time and the ADC start time. This highlights how it is important to pay attention to the inevitable idle times before and after the nominal chirp duration for the practical usage of this radar, an aspect that might be overlooked in purely theoretical studies.

An additional operational requirement for the radar is its angular resolution, which is calculated as

$$a_{\text{res}} = \frac{\lambda}{Nd\cos(\theta)} \tag{5}$$

where $\lambda$ is the wavelength of the radar signal, $d$ is the distance between adjacent antenna elements for the ULA, $\theta$ is the azimuth angle from the boresight, and $N$ is the number of the virtual channel elements in the formed MIMO ULA. To operate multiple channels orthogonally and thus increase the angular resolution, the chosen TI radar board offers TDM and binary phase modulation (BPM) [55]. The TDM mode means that the transmitters will switch ON one after the other to make the signals orthogonal in time dimensions, i.e., only one transmitter is active at any time. Compared with TDM, the BPM approach may suffer from imperfect orthogonality of the added phase modulations and degrade the radar detection performance. Thus, TDM access is commonly used for data collection with this radar board.

## CALIBRATION WITH OTHER SENSORS

Calibrating the radar includes two tasks: one is for time synchronization, and another is for spatial alignment via coordinate transformation. For time synchronization, in this data collection, all the sensors' timing information was stored in the robot operating system framework, except for the radar timing. To address this, the timestamp information is calculated and saved based on the starting recorded time in the radar files and on the chosen pulse repetition time. As the updating rate is different for all sensors, the radar timestamps are taken as a reference, and all other sensor data are sampled at the closest position with respect to the radar timestamps.

In terms of spatial alignment, extrinsic transformations between sensors are formulated relative to the body coordinate frame. Extrinsic sensor calibration can be split into two procedures. First, a relative calibration procedure estimates the sensor's poses relative to all other sensors. Second, an absolute calibration procedure estimates sensor poses with respect to the body coordinate frame of the sensor platform. The calibration of all the sensors except for radar is implemented according to the framework of Domhof et al. [56]. The radar board is installed at measured horizontal and vertical distances to the system in the forward-looking and side-looking regions first. Then, the extrinsic transformations for the Lidar and radar sensors are manually refined and adjusted using a test measurement with a corner reflector. This is an easy target to see with both Lidar and radar, and the related point clouds from the two sensors are manually aligned to be as overlapped as possible as part of this spatial calibration. It is assumed that the extrinsic transformations do not change appreciably between different runs, so only one set of them is needed.

Besides the calibration with other sensors, for the chosen model of the cascaded radar board, an interchannel mismatch calibration is also required to account for frequency, phase, and amplitude mismatch across one single radar chip considered the master, and the other three chips considered the slaves. This calibration is a one-time boresight process using a corner reflector at about 5 m and TDM MIMO configuration. The specific steps of the processing are detailed in [57].

# EXPERIMENTAL RESULTS AND DISCUSSION

## RESULTS FOR IMAGING OF FORWARD-LOOKING DIRECTION

The radar waveform parameters for the forward-looking regions are designed based on the requirements mentioned in the previous section and reported in Table 1. With these waveform parameters, the maximum range is 60 m, the

**Table 1.**

**Radar Parameters for the Experimental Data Collection (Front-Looking Region)**

| Radar Parameters | Symbol | Value |
|---|---|---|
| Starting frequency (GHz) | $F_0$ | 77 |
| Chirp slope (MHz/$\mu$s) | $\mu$ | 30 |
| Sampling rate (Msps) | $F_s$ | 12 |
| Bandwidth (GHz) | $B$ | 0.64 |
| Number of chirps | $L_d$ | 128 |
| PRI (ms) | $T_c$ | 5.5 |
| Number of virtual ULA channels | $N$ | 86 |

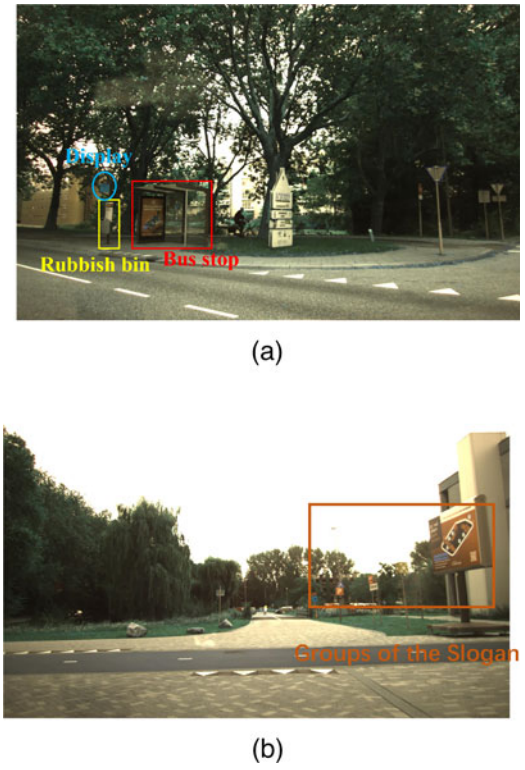


**Figure 4.**
Examples of optical images from the forward-looking camera, with two different scenes in (a) and (b). "Groups of the slogan" denotes multiple vertical posts and a board with a slogan on it.

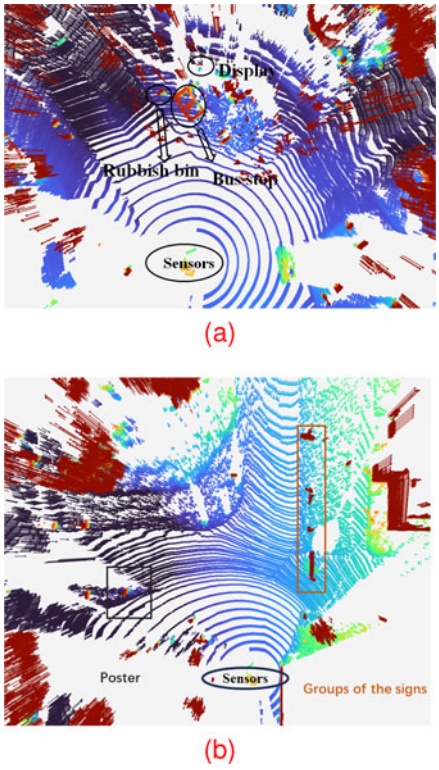


**Figure 5.**
Images from Lidar data corresponding to the two scenes shown in Figure 4. "Groups of the slogan" denotes multiple vertical posts and a board with a slogan on it.

range resolution is 0.23 m, the maximum unambiguous velocity is 4.18 m/s, and the velocity resolution is 0.033 m/s. The angular resolution at boresight with full ULA formed is 1.3°. The TI Cascaded MIMO radar forms an 86-element uniform linear virtual array in one direction, which is used for the processing in this article.

In the following, some representative scenarios and results are presented and discussed. Figures 4 and 5 present two different scenarios as seen by the camera and the Lidar. The imagery in Figure 4(a) from the camera offers an easy empirical interpretation of the scenario, with key targets, such as a bus stop, rubbish bin, and display board, marked in the corresponding figure; the same targets are also marked in the Lidar image in Figure 5(a). In Figure 4(b), another scenario is shown with multiple posts and boards marked, where the poster is not visible because of the limited field of view of the camera, but both targets are marked in the corresponding Lidar image in Figure 5(b).

Figure 6 includes radar images for the first scenario shown in both Figures 4(a) and 5(a) using a different number of virtual channels for DOA and imaging algorithms. Figure 6(a) uses 86 virtual channel elements, essentially equivalent to all those available in the chosen radar sensor. This offers a good spatial resolution of 1.3° at boresight. However, the practical utilization of such a large aperture is unfeasible in realistic vehicles, and additionally, the TDM approach necessary to operate the four independent MIMO radar chips together will further limit the unambiguous estimation of target velocities since the $T_c$ in (2) needs to multiply the number of transmitters used. Thus, in Figure 6 (b) and (c), the results are based on only eight virtual channel elements, which is much easier to achieve for practical automotive radar systems. Figure 6(b) is generated using a conventional imaging approach and provides rough information on the bus stop and rubbish bin targets, making it not straightforward to interpret. With the *3DRUDAT* imaging algorithm proposed in [35], a higher resolution image can be obtained while still keeping the number of virtual channel elements to 8.

Notably, several objects in the scene can be distinguished in the image, whereas they tend to form a broader, uniform signature in the image generated by the conventional imaging algorithm. To provide a quantitative observation, the dynamic range for the bus stop target in Figure 6(b) is measured at -2.3 dB, while in Figure 6(a), this improves to approximately -20 dB. This improvement in sidelobe level is attributed to the accumulated energy from the targets themselves when using more antenna elements, resulting in an improved

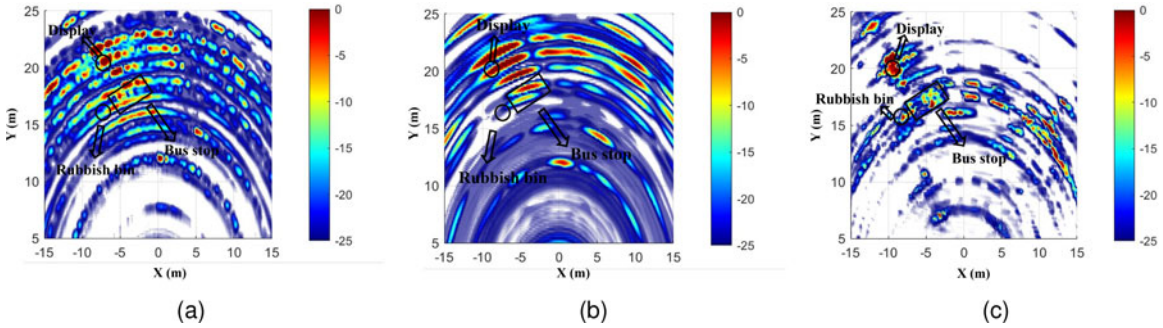


**Figure 6.**
Radar images of the scenario shown in Figures 4(a) and 5(a) with camera and Lidar, respectively. (a) Radar imaging results using all 86 virtual channel elements. (b) Radar imaging results using only eight virtual channel elements. (c) Radar imaging results using eight virtual channel elements with the proposed *3DRUDAT* algorithm [35].

signal-to-noise ratio (SNR). In the case of the proposed method, which enhances SNR through the multiplication of results from DBS and beamforming, the dynamic range in Figure 6(c) is notably low at -30 dB.

The radar-based results presented in Figure 7 for the second scenario, as shown in both Figures 4(b) and 5(b), provide similar trends to compare the different imaging algorithms. The multiple poles and boards and the poster targets appear to be well focused and with more detail in Figure 7(c), compared with the image generated by the conventional MIMO DBF in Figure 7(b). Both subfigures are generated using only eight virtual channel elements. Remarkably, the *3DRUDAT* imaging algorithm appears to also outperform the conventional MIMO DBF imaging using the larger aperture array, with results shown in Figure 7(a) with all the posts well focused with a much narrower main lobe beam.

The image contrast metric is introduced to demonstrate the separation capability of the proposed method. Image contrast quantifies the intensity differences across image pixels and is often used to evaluate sidelobe suppression in SAR images [58], [59]. When two extended targets are better separated due to enhanced angular resolution, the intensity values in the region between them decrease, resulting in a higher image contrast value.

The image contrast $C$ is defined as follows:

$$C = \frac{\sqrt{E\left[I^2(i,j) - E(I^2(i,j))^2\right\}}}{E(I^2(i,j))} \tag{6}$$

where $I^2(i,j)$ is the pixel intensity of $(i,j)$, and $E[\bullet]$ is the mean operation.

In Scene 1, the image contrast using 86 virtual elements, also shown in Figure 6(a), is 2.9078, while using eight virtual elements, as shown in Figure 6(b), yields a value of 2.5387. As expected, the proposed method achieves the highest image contrast, at 4.8642, as also shown in Figure 6(c). A similar trend is observed in Scene 2, where the image contrast for Figure 7(a) is 3.9229, and for Figure 7(b), it is 3.0542, whereas the proposed method achieves the highest image contrast value of 7.4144.

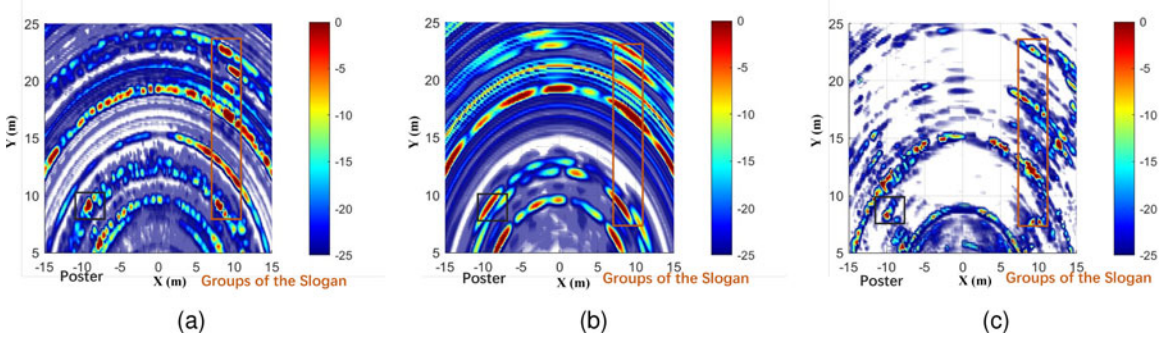


**Figure 7.**
Radar images of the scenario shown in Figures 4(b) and 5(b) with camera and Lidar, respectively ("groups of the slogan" denotes multiple vertical posts and a board with a slogan on it). (a) Radar imaging results using all 86 virtual channel elements. (b) Radar imaging results using only eight virtual channel elements. (c) Radar imaging results using eight virtual channel elements with the proposed *3DRUDAT* algorithm [35].

**Table 2.**

| Radar Parameters for the Experimental Data Collection (Side-Looking Region) | | |
|---|---|---|
| **Radar Parameters** | **Symbol** | Value |
| Starting frequency (GHz) | $F_0$ | 77 |
| Chirp slope (MHz/$\mu$s) | $\mu$ | 30 |
| Sampling rate (Msps) | $F_s$ | 6 |
| Bandwidth (GHz) | $B$ | 1.28 |
| Number of chirps | $L_d$ | 128 |
| PRI (ms) | $T_c$ | 0.9 |
| Number of virtual ULA channels | $N$ | 86 |

The resolution improvement for DOA is given here when the radar is moving at $[v_x, v_y, v_z]$ as

$$n_a = \frac{2N_d T}{N_a d}\cos(\phi)(v_y \tan(\theta) + v_x) \quad (7)$$

$$n_e = \frac{2N_d T}{N_e d}((v_y \cos(\theta) + v_x \sin(\theta))\tan(\phi) + v_z) \quad (8)$$

where $n_a$ and $n_e$ are the resolution improvement terms for azimuth DOA and elevation DOA, respectively. $N_d$ is the number of slow time chirps used for DBS; $N_e$ and $N_a$ are the numbers of antenna elements used for DBF (conventional MIMO) in azimuth and elevation, respectively; $T$ is the pulse repetition time; and $\theta$ and $\phi$ are the targets' position in azimuth and elevation.

## RESULTS FOR IMAGING OF SIDE-LOOKING DIRECTION

The radar waveform parameters for the side-looking region are reported in Table 2. With this waveform designed for a side-looking geometry, the maximum range is 30 m, the range resolution is 0.12 m, the maximum unambiguous velocity is 2.1 m/s, and the velocity resolution is 0.016 m/s.

In the following, figures of representative scenarios and results of radar-based imaging algorithms are presented and discussed. In Figure 8(a), imagery from a GOpro camera offers an easy visual interpretation of the scenario, with two parked cars and a building in the farther background region. The corresponding targets are also marked in the Lidar image, as shown in Figure 9(a). In Figure 8(b), a scene from a parking lot in the TU Delft campus is shown with three parked vehicles highlighted in the foreground, whereas Figure 9(b) shows the same scenario perceived by Lidar where even more cars are visible.

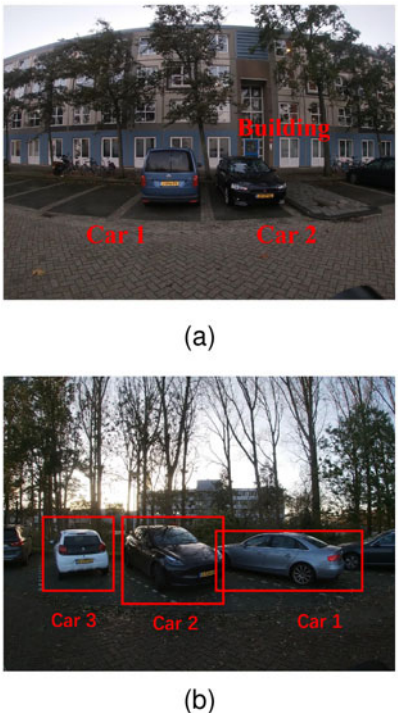


**Figure 8.**
Example of optical images from the side-looking camera, with two different scenes in (a) and (b).

Figure 10 includes radar images for the first scenario shown in Figures 8(a) and 9(a). Figure 10(a) is the result of conventional MIMO processing. Motivated by using a 1D MIMO array in the elevation domain to alleviate the requirement for large radar apertures in-vehicle systems, the following processing is implemented with only one antenna in azimuth. Since only one antenna is used, there is no resolution in the azimuth direction. Figure 10(b) is the result of the imaging algorithm in [60], which uses one single-frame data and 1D antenna array to generate 3D high-resolution imaging results. The two parked cars in the scene and the building in the background are well focused in the image. However, with limited frame data, the results may still be challenging for interpretation and perception tasks. Figure 10(c) presents the result of the conventional BP imaging algorithm for the same scenario but using 49 frames of data. Since the BP algorithm is designed to work in a 2D plane, the images are without elevation information. Figure 10(d) shows the image obtained by the imaging algorithm proposed in [61]. These results use only one antenna element but over 49 frames of data. The method incoherently sums the target information in the imaging field, leading to a three-times faster imaging algorithm compared with the conventional BP algorithm, easing its implementation in realistic contexts. The two cars are well separated, as in

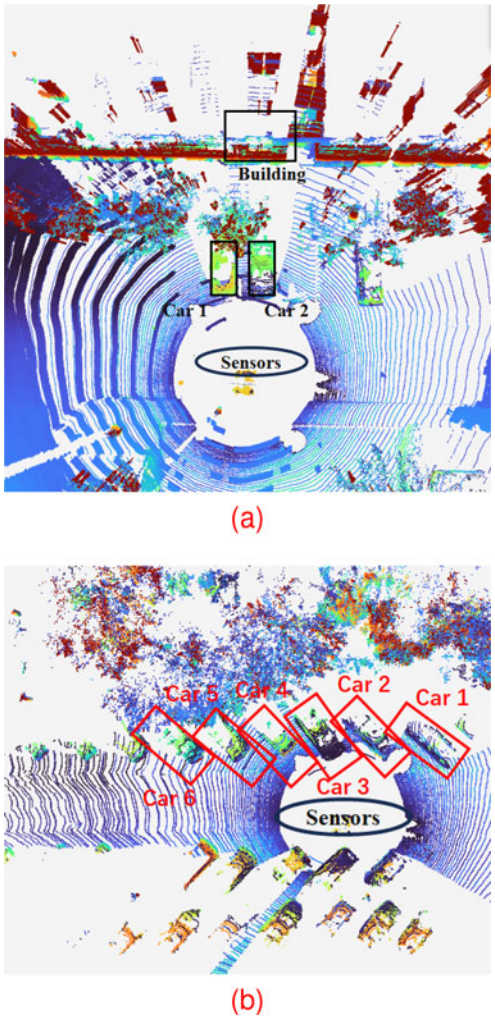


**Figure 9.**
Images from Lidar data corresponding to the two scenes shown in Figure 8.

BP, and have more detailed information than when using only one frame of data. The image contrast in Figure 10(c) is 3.2948, while it is 15.6162 in Figure 10 (d). However, such improvement is not related to the improvement in resolution, but to the fact that the sidelobe and the clutter response are not coherently accumulated with our incoherent imaging method.

Another example is presented in Figure 11. The depicted scenario is the same as that shown in Figure 8 (b) with camera and in Figure 9(b) with Lidar. In Figure 11(b), the three parked cars in the foreground are present in the image, but it is challenging to interpret well the scene and the details of the targets. Similar to the scenario discussed in the previous example, all car targets appear to be better focused when using the conventional BP algorithm in Figure 11(c) and the incoherent processing method of [61] with multiple frames data in Figure 11(d). Specifically, in this example, 200 frames were considered, corresponding to the speed of the car driving at 1 m/s.

As no physical movement is present in the elevation dimension, the angular resolution will remain the same as before. The azimuth resolution improvement for DOA is approximated when the radar is moving at $[v_x, v_y, v_z]$ as

$$n_a \approx \left\lfloor \frac{L_d}{\lfloor \frac{d}{2v_y T} \rfloor} \right\rfloor \frac{1}{N_a} + 1 \tag{9}$$

where $\lfloor \rfloor$ is the rounding operation, $L_d$ is the total number of chirps in one snapshot, $d$ is the distance between different receivers, $v_y$ is the speed of moving directions, $T$ is the chirp duration, and $N_a$ is the number of antenna used for azimuth DOA estimation. It should be noted that $N_a = 1$ for Figures 10(a) and 11(a) as only one azimuth antenna is used.

## DISCUSSION

### WAVEFORM PARAMETERS VERSUS TDM

As mentioned, TDM is the most commonly used method to generate MIMO orthogonal signals for finer angular resolution. However, TDM will lead to problems in automotive scenarios. One of them is the decrease of the maximum measurable velocity, as this parameter, as defined in (2), is determined by the pulse repetition time. For TDM, this time is linearly positively correlated to the number of transmitters, i.e., the more transmitters need to be switched ON/OFF one after the other, the longer that effective repetition time will be.

Orthogonal frequency-division multiplexing in MIMO waveform can potentially avoid the disadvantage of TDM. Different code families, namely, random, Gold, zero correlation zone, and Kasami codes [62] are optimized for periodic auto-correlation properties. However, they still exhibit reasonable a-periodic autocorrelation properties, which means that the orthogonality cannot be achieved perfectly. This will increase the sidelobes and worsen the beam pattern for the MIMO radar system, thus degrading the performance of DOA estimation. Ongoing research work focuses on advanced signal processing methods to address the shrinking range of the unambiguous measurable velocity by using all the transmitted signals in TDM or to design better-coded waveforms for different transmitters to achieve orthogonality.

### INFLUENCE OF MOVING TARGETS

This challenge arises from the movement of targets in the scene. As motion-based high-resolution imaging algorithms are typically based on the relationship between the

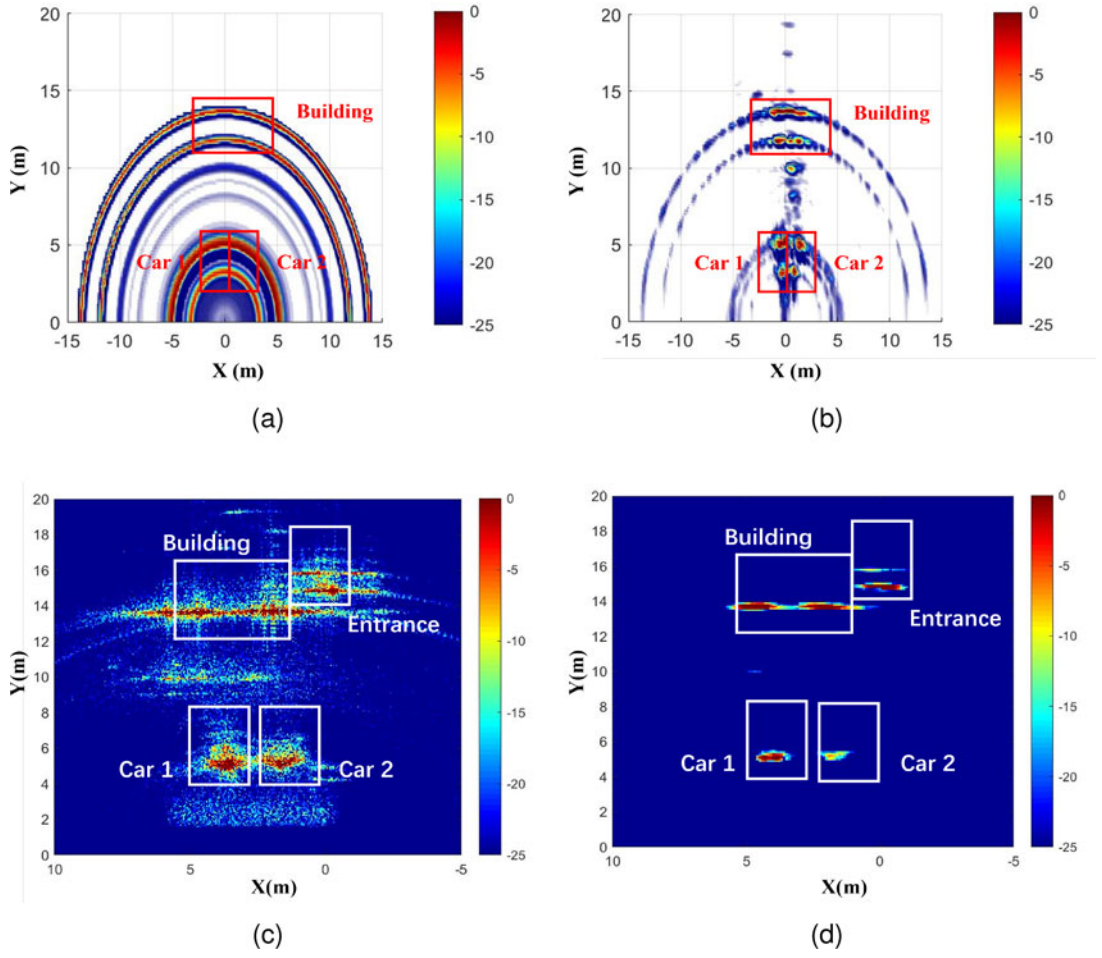


**Figure 10.**
Radar images of the scenario shown in Figures 8(a) and 9(a) with camera and Lidar, respectively. (a) Radar imaging results of conventional MIMO processing. (b) Radar 3D imaging results using a 1D array of one frame data with the algorithm in [60]. (c) Radar 2D imaging results using the BP algorithm with 49 frames of data. (d) Imaging results of 49 frames of data using the first element in the 1D array with the algorithm in [61].

Doppler velocity and the angle of targets, the presence of nonstatic targets will degrade their performance. Furthermore, the targets' movement will accumulate more errors when utilizing multiple frames in the imaging algorithm. To mitigate this effect, static targets and moving targets need to be distinguished and processed using different techniques. Autofocusing algorithms to estimate the target's movement and compensate for this during the imaging processing can be an interesting avenue of research in this context.

## EFFECT OF DRIVING VELOCITY

Motion-based high-resolution imaging algorithms are based on the platform's movement. Depending on the specific implementation of these algorithms, different requirements on the driving velocities that are most suitable to obtain good images will follow. Specifically, algorithms for forward-looking regions, such as [32], [33], [34], and [35], are based on the Doppler profile, which means that the maximum velocity of the targets induced by the motion of the vehicle should be within the maximum unambiguous Doppler velocity as in (2).

The algorithm for side-looking regions, such as [49] and [50], requires enough movement to physically expand the aperture during the frame period; this determines a lower bound of the driving velocity. Moreover, the generated additional motion-enhanced snapshots need to maintain coherence with the existing data from the physical MIMO array; this determines an upper bound of the driving velocity. Both lower and upper values are highly related to the vehicle speed and the duration of the radar chirp, as in

$$V \in \left[\frac{d}{4L_d T_c}, \frac{d}{2T_c}\right] \tag{10}$$

where $V$ is the driving velocity and $d$ is typically assumed to be half wavelength.

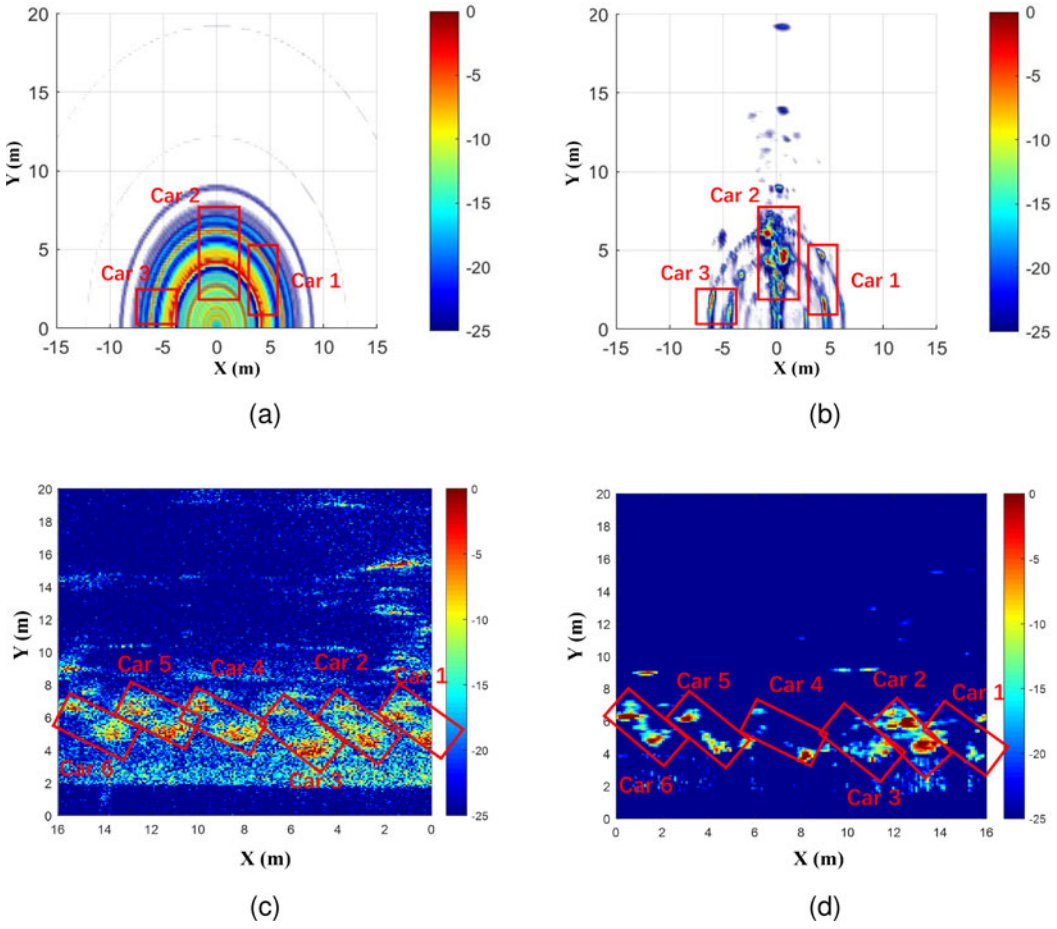


**Figure 11.**
Radar images of the scenario shown in Figures 8(b) and 9(b) with camera and Lidar, respectively. (a) Radar imaging results of conventional MIMO processing. (b) Radar 3D imaging results using a 1D array of one frame data with the algorithm in [60] algorithm. (c) Radar 2D imaging results using the BP algorithm with 200 frames of data. (d) Imaging results of 200 frames of data using the first element in the 1D array with the algorithm in [61].

## CONCLUSION

In this article, an overview of existing resolution-enhancing approaches is provided. Despite the large variety of them, high computational costs and the complex nature of the scene, including clutter, place limits on their practical usage. At the same time, high-resolution imaging algorithms that exploit the movement of the vehicle have large potential, which has been demonstrated with examples for both the forward-looking regions and the side-looking regions. Experimental data collected in real driving scenarios in the city of Delft, The Netherlands, have been used to showcase the performances of the algorithms. Specifically, it has been validated how some of these algorithms improve the angular resolution to estimate targets' positions and, consequently, the quality of the obtained images. In the analysis part, some of the important practical aspects for the implementation and applicability of imaging algorithms in realistic driving scenarios have also been listed and discussed. These are important to account for when moving from simulations of relatively simple scenes to practical automotive radar scenarios.

## ACKNOWLEDGMENTS

The authors would like to thank the China Scholarship Council (CSC) for the PhD scholarship of Sen Yuan. The authors are also grateful to I. Roldan, A. Palffy, and the joint team of the MS3 and Intelligent Vehicles (IV) groups of TU Delft for organizing the experimental data collection and making data available.

## REFERENCES

[1] S. M. Patole, M. Torlak, D. Wang, and M. Ali, "Automotive radars: A review of signal processing techniques," vol. 34, no. 2, pp. 22–35, Mar. 2017, doi: 10.1109/MSP.2016.2628914. [Online]. Available: https://ieeexplore.ieee.org/document/7870764/

[2] F. Roos, J. Bechter, C. Knill, B. Schweizer, and C. Waldschmidt, "Radar sensors for autonomous driving: Modulation schemes and interference mitigation," *IEEE Microw. Mag.*, vol. 20, no. 9, pp. 58–72, Sep. 2019, doi: 10.1109/MMM.2019.2922120.

[3] S. Sun, A. P. Petropulu, and H. V. Poor, "MIMO radar for advanced driver-assistance systems and autonomous driving: Advantages and challenges," *IEEE Signal Process. Mag.*, vol. 37, no. 4, pp. 98–117, Jul. 2020, doi: 10.1109/MSP.2020.2978507.

[4] P. Barton, "Digital beam forming for radar," *IEE Proc. F (Commun., Radar Signal Process.)*, vol. 127, no. 4, pp. 266–277, Aug. 1980, doi: 10.1049/ip-f-1.1980.0041.

[5] J. Capon, "High-resolution frequency-wavenumber spectrum analysis," *Proc. IEEE*, vol. 57, no. 8, pp. 1408–1418, Aug. 1969, doi: 10.1109/PROC.1969.7278.

[6] S. Xu, J. Wang, and A. Yarovoy, "Super resolution DOA for FMCW automotive radar imaging," in *Proc. 2018 IEEE Conf. Antenna Meas. Appl.*, 2018, pp. 1–4, doi: 10.1109/CAMA.2018.8530609.

[7] S. Xu and A. Yarovoy, "Joint Doppler and DOA estimation using 2D music in presence of phase residual," in *Proc. Eur. Radar Conf.*, 2017, pp. 203–206, doi: 10.23919/EURAD.2017.8249182.

[8] R. Roy and T. Kailath, "ESPRIT-estimation of signal parameters via rotational invariance techniques," *IEEE Trans. Acoust., Speech, Signal Process.*, vol. 37, no. 7, pp. 984–995, Jul. 1989, doi: 10.1109/29.32276.

[9] Y. Fang, S. Zhu, C. Zeng, Y. Gao, and S. Li, "DOA estimations with limited snapshots based on improved rank-one correlation model in unknown nonuniform noise," *IEEE Trans. Veh. Technol.*, vol. 70, no. 10, pp. 10308–10319, Oct. 2021, doi: 10.1109/TVT.2021.3105673.

[10] C. Zeng, S. Zhu, S. Li, Q. Liao, and L. Wang, "Sparse frame DOA estimations via a rank-one correlation model for low SNR and limited snapshots," *Appl. Comput. Harmon. Anal.*, vol. 41, no. 2, pp. 362–383, 2016, doi: 10.1016/j.acha.2016.02.002.

[11] T.-J. Shan, M. Wax, and T. Kailath, "On spatial smoothing for direction-of-arrival estimation of coherent signals," *IEEE Trans. Acoust., Speech, Signal Process.*, vol. 33, no. 4, pp. 806–811, Aug. 1985, doi: 10.1109/TASSP.1985.1164649.

[12] W. Liao and A. Fannjiang, "MUSIC for single-snapshot spectral estimation: Stability and super-resolution," *Appl. Comput. Harmon. Anal.*, vol. 40, no. 1, pp. 33–67, 2016, doi: 10.1016/j.acha.2014.12.003.

[13] Y. Ma, Y. Zeng, and S. Sun, "A deep learning based super resolution DoA estimator with single snapshot MIMO radar data," *IEEE Trans. Veh. Technol.*, vol. 71, no. 4, pp. 4142–4155, Apr. 2022, doi: 10.1109/TVT.2022.3151674.

[14] S. Fortunati, R. Grasso, F. Gini, M. S. Greco, and K. LePage, "Single-snapshot DOA estimation by using compressed sensing," *EURASIP J. Adv. Signal Process.*, vol. 2014, no. 1, pp. 1–17, 2014, doi: 10.1186/1687-6180-2014-120.

[15] K. Srinivas, S. Ganguly, and P. K. Kumar, "Performance comparison of reconstruction algorithms in compressive sensing based single snapshot DOA estimation," *IETE J. Res.*, vol. 68, pp. 1–9, 2020, doi: 10.1080/03772063.2020.1732840.

[16] W. Roberts, P. Stoica, J. Li, T. Yardibi, and F. A. Sadjadi, "Iterative adaptive approaches to MIMO radar imaging," *IEEE J. Sel. Topics Signal Process.*, vol. 4, no. 1, pp. 5–20, Feb. 2010, doi: 10.1109/JSTSP.2009.2038964.

[17] T. Yardibi, J. Li, P. Stoica, M. Xue, and A. B. Baggeroer, "Source localization and sensing: A nonparametric iterative adaptive approach based on weighted least squares," *IEEE Trans. Aerosp. Electron. Syst.*, vol. 46, no. 1, pp. 425–443, Jan. 2010, doi: 10.1109/TAES.2010.5417172.

[18] W. Wei et al., "DOA estimation of distributed mmWave radar system via fast iterative adaptive approach," in *Proc. 2021 Int. Conf. Control, Autom. Inf. Sci.*, 2021, pp. 414–418, doi: 10.1109/ICCAIS52680.2021.9624547.

[19] E. Aboutanios, A. Hassanien, M. G. Amin, and A. M. Zoubir, "Fast iterative interpolated beamforming for accurate single-snapshot DOA estimation," *IEEE Geosci. Remote Sens. Lett.*, vol. 14, no. 4, pp. 574–578, Apr. 2017, doi: 10.1109/LGRS.2017.2661315.

[20] F. Roos et al., "Compressed sensing based single snapshot DoA estimation for sparse MIMO radar arrays," in *Proc. 2019 12th German Microw. Conf.*, 2019, pp. 75–78, doi: 10.23919/GEMIC.2019.8698136.

[21] R. Cao, B. Liu, F. Gao, and X. Zhang, "A low-complex one-snapshot DOA estimation algorithm with massive ULA," *IEEE Commun. Lett.*, vol. 21, no. 5, pp. 1071–1074, May 2017, doi: 10.1109/LCOMM.2017.2652442.

[22] G. W. Stimson, *Introduction to Airborne Radar*. Raleigh, NC, USA: SciTech Publishing, Inc., 1998, doi: 10.1049/SBRA101E.

[23] D. Mao, Y. Zhang, Y. Zhang, Y. Huang, and J. Yang, "Doppler beam sharpening using estimated Doppler centroid based on edge detection and fitting," *IEEE Access*, vol. 7, pp. 123604–123615, 2019, doi: 10.1109/ACCESS.2019.2937992.

[24] S. Chen, Y. Yuan, S. Zhang, H. Zhao, and Y. Chen, "A new imaging algorithm for forward-looking missile-borne bistatic SAR," *IEEE J. Sel. Topics Appl. Earth Observ. Remote Sens.*, vol. 9, no. 4, pp. 1543–1552, Apr. 2016, doi: 10.1109/JSTARS.2015.2507260.

[25] M. Bao, P. Zhou, and L. Shi, "Study on deambiguity algorithm for double antenna forward looking missile borne SAR," *J. Electron. Inf. Technol.*, vol. 35, no. 12, pp. 2857–2862, 2013, doi: 10.3724/SP.J.1146.2013.00083.

[26] M. Zhang, G. Liao, X. He, and S. Zhu, "Unambiguous forward-looking SAR imaging on HSV-R using frequency diverse array," *Sensors*, vol. 20, no. 4, 2020, Art. no. 1169, doi: 10.3390/s20041169.

[27] Y. Zhang, D. Mao, Y. Zhang, Y. Huang, and J. Yang, "Multi-beam Doppler beam sharpening approach for airborne forward-looking radar imaging," in *Proc. 2017 IEEE Int. Geosci. Remote Sens. Symp.*, 2017, pp. 6142–6145, doi: 10.1109/IGARSS.2017.8128410.

[28] J. Lu, L. Zhang, P. Xie, Z. Meng, and Y. Cao, "High-resolution imaging of multi-channel forward-looking synthetic aperture radar under curve trajectory," *IEEE Access*, vol. 7, pp. 51211–51221, 2019, doi: 10.1109/ACCESS.2019.2911554.

[29] A. Albaba, M. Bauduin, T. Verbelen, H. Sahli, and A. Bourdoux, "Forward-looking MIMO-SAR for enhanced radar imaging in autonomous mobile robots," *IEEE Access*, vol. 11, pp. 66934–66948, 2023, doi: 10.1109/ACCESS.2023.3291611.

[30] A. Albaba, A. Sakhnini, H. Sahli, and A. Bourdoux, "Forward-looking MIMO-SAR for enhanced angular resolution," in *Proc. 2022 IEEE Radar Conf.*, 2022, pp. 1–6, doi: 10.1109/RadarConf2248738.2022.9764255.

[31] A. Albaba, M. Bauduin, A. Sakhnini, H. Sahli, and A. Bourdoux, "Sidelobes and ghost targets mitigation technique for high-resolution forward-looking MIMO-SAR," *IEEE Trans. Radar Syst.*, vol. 2, pp. 237–250, 2024, doi: 10.1109/TRS.2024.3366779.

[32] S. L. Cassidy, S. Pooni, M. Cherniakov, E. G. Hoare, and M. S. Gashinova, "High resolution automotive imaging using MIMO radar and Doppler beam sharpening," *IEEE Trans. Aerosp. Electron. Syst.*, vol. 59, no. 2, pp. 1495–1505, Apr. 2023, doi: 10.1109/TAES.2022.3203953.

[33] S. Yuan, P. Aubry, F. Fioranelli, and A. Yarovoy, "A novel approach to unambiguous Doppler beam sharpening for forward-looking MIMO radar," *IEEE Sensors J.*, vol. 22, no. 23, pp. 23494–23506, Dec. 2022, doi: 10.1109/JSEN.2022.3215862.

[34] S. Yuan, F. Fioranelli, and A. Yarovoy, "An adaptive threshold-based unambiguous robust Doppler beam sharpening algorithm for forward-looking MIMO radar," in *Proc. 2023 20th Eur. Radar Conf.*, 2023, pp. 65–68, doi: 10.23919/EuRAD58043.2023.10288626.

[35] S. Yuan, F. Fioranelli, and A. Yarovoy, "3DRUDAT: 3D robust unambiguous Doppler beam sharpening using adaptive threshold for forward-looking region," *IEEE Trans. Radar Syst.*, vol. 2, pp. 138–153, 2024, doi: 10.1109/TRS.2024.3353202.

[36] W. Zhang, P. Wang, N. He, and Z. He, "Super resolution DOA based on relative motion for FMCW automotive radar," *IEEE Trans. Veh. Technol.*, vol. 69, no. 8, pp. 8698–8709, Aug. 2020, doi: 10.1109/TVT.2020.2999640.

[37] X. Gao, S. Roy, and G. Xing, "MIMO-SAR: A hierarchical high-resolution imaging algorithm for mmWave FMCW radar in autonomous driving," *IEEE Trans. Veh. Technol.*, vol. 70, no. 8, pp. 7322–7334, Aug. 2021, doi: 10.1109/TVT.2021.3092355.

[38] S. Yuan, F. Fioranelli, and A. Yarovoy, "An approach for high-angular resolution implementation in moving automotive MIMO radar," in *Proc. 2021 18th Eur. Radar Conf.*, 2022, pp. 449–452, doi: 10.23919/EuRAD50154.2022.9784507.

[39] H. Iqbal, A. Löffler, M. N. Mejdoub, D. Zimmermann, and F. Gruson, "Imaging radar for automated driving functions," *Int. J. Microw. Wireless Technol.*, vol. 13, pp. 682-690, 2021, doi: 10.1017/S1759078721000465.

[40] M. Manzoni et al., "Residual motion compensation in automotive MIMO SAR imaging," in *Proc. IEEE Radar Conf.*, New York City, NY, USA, 2022, pp. 1–7, doi: 10.1109/RadarConf2248738.2022.9764310.

[41] S. Xu, B. J. Kooij, and A. Yarovoy, "Joint Doppler and DOA estimation using (ultra-) wideband FMCW signals," *Signal Process.*, vol. 168, 2020, Art. no. 107259, doi: 10.1016/j.sigpro.2019.107259.

[42] S. Xu and A. Yarovoy, "Joint features extraction for multiple moving targets using (ultra-) wideband FMCW signals in the presence of Doppler ambiguity," *IEEE Trans. Signal Process.*, vol. 68, pp. 6562–6577, 2020, doi: 10.1109/TSP.2020.3039565.

[43] M. L. L. d. Oliveira and M. J. Bekooij, "Deep-MLE: Fusion between a neural network and MLE for a single snapshot DOA estimation," in *Proc. 2022-2022 IEEE Int. Conf. Acoust., Speech Signal Process.*, 2022, pp. 3673–3677, doi: 10.1109/ICASSP43922.2022.9747692.

[44] C. Liu, W. Feng, H. Li, and H. Zhu, "Single snapshot DOA estimation based on spatial smoothing MUSIC and CNN," in *Proc. 2021 IEEE Int. Conf. Signal Process., Commun. Comput.*, 2021, pp. 1–5, doi: 10.1109/ICSPCC52875.2021.9564893.

[45] M. L. L. d. Oliveira and M. J. Bekooij, "ResNet applied for a single-snapshot DOA estimation," in *Proc. 2022 IEEE Radar Conf.*, 2022, pp. 1–6, doi: 10.1109/RadarConf2248738.2022.9763905.

[46] I. Roldan, F. Fioranelli, and A. Yarovoy, "Enhancing angular resolution using neural networks in automotive radars," in *Proc. 2021 18th Eur. Radar Conf.*, 2022, pp. 58–61, doi: 10.23919/EuRAD50154.2022.9784559.

[47] G. Qin, M. G. Amin, and Y. D. Zhang, "DOA estimation exploiting sparse array motions," *IEEE Trans. Signal Process.*, vol. 67, no. 11, pp. 3013–3027, Jun. 2019, doi: 10.1109/TSP.2019.2911261.

[48] S. Li and X.-P. Zhang, "A new approach to construct virtual array with increased degrees of freedom for moving sparse arrays," *IEEE Signal Process. Lett.*, vol. 27, pp. 805–809, 2020, doi: 10.1109/LSP.2020.2993956.

[49] S. Yuan, F. Fioranelli, and A. Yarovoy, "Vehicular motion-based DOA estimation with a limited amount of snapshots for automotive MIMO radar," *IEEE Trans. Aerosp. Electron. Syst.*, vol. 59, no. 6, pp. 7611–7625, Dec. 2023, doi: 10.1109/TAES.2023.3291335.

[50] S. Yuan, F. Fioranelli, and A. Yarovoy, "3D high-resolution imaging algorithm using 1D MIMO array for autonomous driving application," *IEEE Trans. Radar Syst.*, vol. 2, pp. 1186–1199, 2024, doi: 10.1109/TRS.2024.3493992.

[51] T. I. Inc, "Design guide: Tidep-01012—imaging radar using cascaded mmWave sensor reference design (rev. a)," 2019. [Online]. Available: https://www.ti.com/lit/ug/tiduen5a/tiduen5a.pdf

[52] G. Hakobyan and B. Yang, "High-performance automotive radar: A review of signal processing algorithms and modulation schemes," *IEEE Signal Process. Mag.*, vol. 36, no. 5, pp. 32–44, Sep. 2019, doi: 10.1109/MSP.2019.2911722. [Online]. Available: https://ieeexplore.ieee.org/document/8828004/

[53] F. Engels, P. Heidenreich, A. M. Zoubir, F. K. Jondral, and M. Wintermantel, "Advances in automotive radar: A framework on computationally efficient high-resolution frequency estimation," *IEEE Signal Process. Mag.*, vol. 34, no. 2, pp. 36–46, Mar. 2017, doi: 10.1109/MSP.2016.2637700. [Online]. Available: https://ieeexplore.ieee.org/document/7870737/

[54] I. Bilik, O. Longman, S. Villeval, and J. Tabrikian, "The rise of radar for autonomous vehicles," *IEEE Signal Process. Mag.*, vol. 36, no. 5, pp. 20–31, Sep. 2019, doi: 10.1109/MSP.2019.2926573.

[55] S. Rao, "MIMO radar (rev. a) - Texas Instruments India Application Report," 2018. [Online]. Available: https://www.ti.com/lit/pdf/swra554

[56] J. Domhof, J. F. Kooij, and D. M. Gavrila, "A joint extrinsic calibration tool for radar, camera and lidar," *IEEE Trans. Intell. Veh.*, vol. 6, no. 3, pp. 571–582, Sep. 2021, doi: 10.1109/TIV.2021.3065208.

[57] T. I. Inc, "mmWave studio cascade users guide 2," 2020. [Online]. Available: https://dr-download.ti.com/software-development/ide-configuration-compiler-or-debugger/MD-h04ItoajtS/02.01.00.00/mmwave_studio_cascade_user_guide.pdf

[58] S. Yuan, Z. Yu, C. Li, and S. Wang, "A novel SAR sidelobe suppression method based on CNN," *IEEE Geosci. Remote Sens. Lett.*, vol. 18, no. 1, pp. 132–136, Jan. 2021, doi: 10.1109/LGRS.2020.2968336.

[59] F. Berizzi and G. Corsini, "Autofocusing of inverse synthetic aperture radar images using contrast optimization," *IEEE Trans. Aerosp. Electron. Syst.*, vol. 32, no. 3, pp. 1185–1191, Jul. 1996, doi: 10.1109/7.532282.

[60] S. Yuan, S. Zhu, F. Fioranelli, and A. Yarovoy, "3-D egomotion estimation using multi-channel FMCW radar," *IEEE Trans. Radar Syst.*, vol. 1, pp. 368–381, 2023, doi: 10.1109/TRS.2023.3299180.

[61] S. Yuan, F. Fioranelli, and A. Yarovoy, "Speeding up imaging over BP for automotive radar: High-resolution algorithm with multi-frame data," in *Proc. 2024 21st Eur. Radar Conf.*, 2024, pp. 204–207, doi: 10.23919/EuRAD61604.2024.10734973.

[62] F. Uysal and S. Orru, "Phase-coded FMCW automotive radar: Application and challenges," in *Proc. 2020 IEEE Int. Radar Conf.*, 2020, pp. 478–482, doi: 10.1109/RADAR42522.2020.9114798.